EPJ B
Condensed Matter and Complex Systems
www.epj.org

Eur. Phys. J. B **67**, 527–542 (2009) DOI: 10.1140/epjb/e2009-00036-4

Transport through quantum dots: a combined DMRG and embedded-cluster approximation study

F. Heidrich-Meisner, G.B. Martins, C.A. Büsser, K.A. Al-Hassanieh, A.E. Feiguin, G. Chiappe, E.V. Anda and E. Dagotto

EDP SCIENCES
Società Italiana di Fisica
Springer

Eur. Phys. J. B **67**, 527–542 (2009)
DOI: 10.1140/epjb/e2009-00036-4

THE EUROPEAN PHYSICAL JOURNAL B

Regular Article

Transport through quantum dots: a combined DMRG and embedded-cluster approximation study

F. Heidrich-Meisner[1,2,a], G.B. Martins[3], C.A. Büsser[3,4], K.A. Al-Hassanieh[1,2,5,11], A.E. Feiguin[6,7], G. Chiappe[8,9], E.V. Anda[10], and E. Dagotto[1,2]

[1] Materials Science and Technology Division, Oak Ridge National Laboratory, Tennessee 37831, USA
[2] Department of Physics and Astronomy, University of Tennessee, Knoxville, 37996 Tennessee, USA
[3] Department of Physics, Oakland University, Rochester, 48309 Michigan, USA
[4] Department of Physics and Astronomy, Ohio University, Athens, 45701 Ohio, USA
[5] National High Magnetic Field Laboratory and Department of Physics, Florida State University, Tallahassee, 32306 FL, USA
[6] Microsoft Project Q, University of California, Santa Barbara, 93106 CA, USA
[7] Condensed Matter Theory Center, Department of Physics, University of Maryland, 20742 MD, USA
[8] Departmento de Física J.J. Giambiagi, Universidad de Buenos Aires, 1428 Buenos Aires, Argentina
[9] Departamento de Física Aplicada, Universidad de Alicante, San Vicente del Raspeig, 03690 Alicante, Spain
[10] Departamento de Física, Pontificia Universidade Católica do Rio de Janeiro, 38071 Rio de Janeiro, Brazil
[11] Theoretical Division T-11, Los Alamos National Laboratory, Los Alamos, NM 87545, USA

Received 7 June 2008 / Received in final form 5 November 2008
Published online 10 February 2009 –

Abstract. The numerical analysis of strongly interacting nanostructures requires powerful techniques. Recently developed methods, such as the time-dependent density matrix renormalization group (tDMRG) approach or the embedded-cluster approximation (ECA), rely on the numerical solution of clusters of finite size. For the interpretation of numerical results, it is therefore crucial to understand finite-size effects in detail. In this work, we present a careful finite-size analysis for the examples of one quantum dot, as well as three serially connected quantum dots. Depending on "odd-even" effects, physically quite different results may emerge from clusters that do not differ much in their size. We provide a solution to a recent controversy over results obtained with ECA for three quantum dots. In particular, using the optimum clusters discussed in this paper, the parameter range in which ECA can reliably be applied is increased, as we show for the case of three quantum dots. As a practical procedure, we propose that a comparison of results for static quantities against those of quasi-exact methods, such as the ground-state density matrix renormalization group (DMRG) method or exact diagonalization, serves to identify the optimum cluster type. In the examples studied here, we find that to observe signatures of the Kondo effect in finite systems, the best clusters involving dots and leads must have a total z-component of the spin equal to zero.

PACS. 73.63.-b Electronic transport in nanoscale materials and structures – 73.63.Kv Quantum dots – 71.27.+a Strongly correlated electron systems; heavy fermions

1 Introduction

The prediction and experimental observation of the Kondo effect in quantum dots [1–4] and single-molecule conductors has stimulated considerable interest in strongly correlated nano-scale systems, as discussed in recent reviews [5–7]. The related experimental and theoretical efforts are not only motivated by novel emerging physical phenomena, but also by the possible technological applications of nanodevices, and in particular by their transport properties. Experimental results for the conductance through nanostructures have been reported for single dots, side and linearly coupled two dots, as well as small molecules [1,8,9].

Stimulated by the rich physics harbored by interacting nanostructures, the field has seen a rapid development of powerful numerical techniques to obtain the conductance. These include the well-established numerical-renormalization group approach (NRG) [10–13], various density-matrix renormalization group (DMRG) based methods [14–16], including in particular, the recently developed time-dependent DMRG (tDMRG) [17–22], Quantum Monte Carlo simulations (see, e.g., Ref. [23]), flow-equation approaches [24], as well as exact diagonalization

[a] *Present address*: Institut für Theoretische Physik C, RWTH Aachen University, 52056 Aachen, Germany.
e-mail: fabian.heidrich-meisner@physik.rwth-aachen.de

combined with an embedding procedure, the embedded-cluster approximation (ECA) [25–28]. We wish to distinguish the latter method from other cluster-embedding approaches used in this field, sometimes dubbed the embedding method [29–31].

Beyond numerical methods, there are many analytical techniques to the problem of transport in quantum dots, ranging from perturbative schemes (see, e.g., Refs. [32–34]), real-time renormalization methods [35], and functional renormalization group approaches [36,37], to slave-boson calculations [38], and variational methods [39,40], just to mention a few. Furthermore, density functional theory (DFT) is widely used to model molecular conductors (see, e.g., Ref. [41] for a review). Such DFT-based approaches successfully account for the coupling of the leads to extended molecules by tackling the molecule plus a substantial part of the leads (see, e.g., Refs. [42,43]). In that sense, there is a similarity with the embedded-cluster approximation, as will become more obvious in the discussion of ECA in Section 2.2. While DFT based methods have been shown to correctly describe Coulomb-blockade physics [42], interacting resonant level models [44], and finite-bias phenomena [43,45], the effects of strong correlations as manifest in the Kondo effect still seem to be out of reach for current DFT schemes. In that sense, DFT based methods are complimentary to other approaches mentioned here that emphasize the effect of strong correlations.

Time-dependent DMRG and ECA are particularly promising methods to address complex nanoscale systems such as molecular conductors. Both methods can in principle include the modeling of phonons, and we mention, as an example, the ECA study reference [46] on a molecular conductor with a center-of-mass motion. Other applications of ECA on timely problems of experimental significance include studies of nonlocal spin control in quantum dots [47], the SU(4) Kondo effect [48], and multilevel quantum dots [49]. Furthermore, it is one of the advantages of DMRG [50–53] and ECA that spatial correlations can be analyzed not only within the interacting region, but also throughout the entire system. Therefore, it is possible to study how the screening of the magnetic moment of quantum dots occurs, which relates to the notion of the so-called *Kondo cloud* [54–57]. The computation of extended spatial correlations within NRG has become possible only recently [58]. Moreover, existing codes for both ECA and tDMRG can easily be adapted to different problems, and ECA calculations can be performed at low computational costs, i.e., the requirements in CPU time needed are rather modest compared to DMRG and NRG. This is, compared to NRG, of particular advantage in the case of multi-channel problems, such as realized in the case of three quantum dots.

As both DMRG and ECA are based on real-space schemes, for the interpretation of numerical results, it is crucial to understand how subtle many-body effects, such as the Kondo effect, manifest themselves on finite systems. It is the purpose of this work to present a detailed analysis of the properties of strongly interacting nanostructures

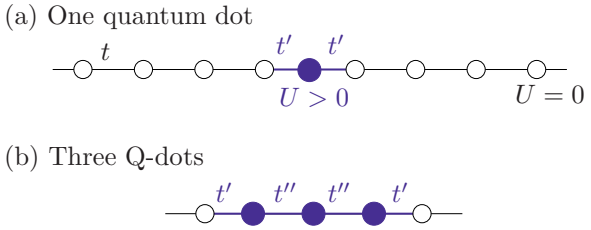

Fig. 1. (Color online) Sketch of the models studied in this work: (a) a single quantum dot embedded into noninteracting leads; (b) three serially coupled dots embedded into leads. Full symbols denote dots (namely, sites with a finite onsite Coulomb repulsion $U > 0$), while open symbols represent tight-binding sites.

and their finite-size scaling, in both DMRG and ECA calculations. Our work first provides a discussion of the one-dot case and then covers three serially coupled quantum dots as well. The models are depicted in Figure 1.

We discuss how the emergence of Kondo physics is reflected in static properties, such as spin and charge fluctuations and spin-spin correlations. In addition, we discuss the conductance of these structures, obtained with the ECA method, as a function of model parameters and gate voltage, which controls the dots' filling. As our main result, we argue that it is important to consider the geometric properties and global quantum numbers of finite systems in order to correctly interpret the results from exact diagonalization (ED)-based approaches such as ECA. The main conclusions are relevant as well for real-time simulations within tDMRG performed with tight-binding leads. We mainly gauge our results against the most established methods, the Bethe ansatz solution of the single impurity problem [59,60], sum rules valid for Fermi liquids [61], and, for multi-dot structures, NRG [13].

The existence of odd-even effects in NRG calculations, which use logarithmically discretized leads (sometimes called Wilson chains, see, e.g., Refs. [16,22]), has been emphasized by Wilson [10], with the important observation that the renormalization procedure of NRG on Wilson chains results in two different fixed points, depending on whether the number of NRG iterations is odd or even. In this work, we discuss odd-even effects that emerge in the finite-size scaling of, e.g., the conductance, when the dot is coupled to leads in a real-space representation [62]. Such even-odd effects and, more generally, the relevance of boundary conditions for transport, have been studied before, e.g., for small chains of dots coupled to wires [63], or quantum box problems [64]. The purpose of our work is to discuss these effects with a perspective on the two methods of interest here, i.e., tDMRG and ECA, and most importantly, on the calculation of conductances for the single-impurity Anderson impurity model and a three-quantum dot model. We mention that even-odd effects and their influence on the conductance have previously been studied by static DMRG in reference [29]. The model studied there was spinless fermions interacting in a constrained region embedded in noninteracting leads in a ring geometry.

The case of three dots [27,28,36,40,65–70] has attracted considerable attention from the theoretical side. Most studies find perfect conductance through the dots at half filling, independently of model parameters such as hopping matrix elements between the dots and onsite Coulomb repulsion [36,40,65–69]. This result is at odds with earlier results obtained from ECA since a conductance dip has been reported in reference [28]. Here, we resolve this issue in favor of the picture promoted in references [36,40,65–69] and show that the controversial dip is not due to a general incapability of ECA to capture the essential physics, but due to quite subtle finite-size effects which have not been appreciated in some earlier ECA calculations [28].

The ECA method incorporates the numerical solution of a small cluster that contains the interacting region – e.g., a quantum dot – by means of exact diagonalization. One example of a relevant global quantum number of such small clusters is $S^z_{\rm total}$, the z-component of the total spin. We illustrate that in certain cases, clusters with an overall $S^z_{\rm total} \neq 0$, at half filling, and with open boundary conditions may exhibit qualitatively different properties from those with $S^z_{\rm total} = 0$. Furthermore, as a practical procedure, we propose that a quantitative comparison of static properties, such as charge variations with gate potential, between ECA and ground-state DMRG or the Lanczos algorithm, allows us to determine the optimum cluster-type for a given model. A Lanczos solver is part of standard ECA codes as we shall explain later.

The Hamiltonian common to the systems analyzed here consists of three parts: the noninteracting leads $H_{\rm leads}$, the coupling between the interacting region and the leads, $H_{\rm hy}$, and the interacting region described by $H_{\rm int}$:

$$H = H_{\rm leads} + H_{\rm hy} + H_{\rm int}, \tag{1}$$

where the leads are described by:

$$H_{\rm leads} = -t \sum_{l=1}^{N_L-1} \left[c^\dagger_{l,\sigma} c_{l+1,\sigma} + \text{h.c.}\right] - t \sum_{l=N_L+N_{\rm int}+1}^{N-1} \left[c^\dagger_{l,\sigma} c_{l+1,\sigma} + \text{h.c.}\right]. \tag{2}$$

As usual, $c^{(\dagger)}_{l,\sigma}$ denotes a fermion annihilation (creation) operator acting on site l, with a spin index $\sigma = \uparrow, \downarrow$. Summation over a repeated index σ is implied throughout the paper. $n_{l,\sigma} = c^\dagger_{l,\sigma} c_{l,\sigma}$ is the local particle operator with spin σ and $n_l = n_{l,\uparrow} + n_{l,\downarrow}$ is the particle number (or charge) operator on site l. The total system size is $N = N_L + N_{\rm int} + N_R$, where $N_{L(R)}$ is the number of sites in the left (right) lead and $N_{\rm int}$ is the number of interacting sites in the center of the system. The hybridization term can be written as:

$$H_{\rm hy} = -t' \sum_\sigma \left(c^\dagger_{N_L,\sigma} c_{N_L+1,\sigma} + c^\dagger_{x,\sigma} c_{x+1,\sigma} + \text{h.c.}\right), \tag{3}$$

with $x = N_L + N_{\rm int}$. Unless otherwise stated, $t = 1$ is the unit of energy. The quantum of conductance in this notation is thus $G_0 = 2$, where the factor of two is due to the two spin channels.

The rest of the paper is organized as follows. In Section 2, we introduce the two methods used here, DMRG and ECA. In Section 3, we revisit the case of a single quantum dot. We point out that tDMRG calculations result in quite different behaviors, depending on the type of open clusters. We qualitatively discuss spin-spin correlations and calculate the conductance as a function of gate voltage with ECA. In Section 4, we present our numerical results for static properties of three quantum dots obtained from DMRG and ECA calculations, with a special focus on their finite-size dependence. This allows us to identify the optimum clusters for the calculation of dynamic properties and the conductance. Section 5 provides a summary and conclusions.

2 Methods

2.1 Time-dependent DMRG

For ground-state DMRG calculations, we use the finite-system size algorithm [52] and we give the number of states M used in either the figures' captions or in the text. The set-up for our adaptive time-dependent DMRG [71,72] calculations of transport properties has been detailed in reference [17]. Here we just repeat that the current $J(\tau)$ (where τ denotes time in units of $1/t$) is measured as the current across the link between the leads and the interacting region (see Eq. (3)):

$$j_{x,x+1} = -it' \sum_\sigma \left(c^\dagger_{x+1,\sigma} c_{x,\sigma} - \text{h.c.}\right)$$
$$J = \left(\langle j_{N_L+N_{\rm int},N_L+N_{\rm int}+1}\rangle_\tau + \langle j_{N_L,N_L+1}\rangle_\tau\right)/2 \tag{4}$$

with $x = N_L + N_{\rm int}$ or $x = N_L$. $\langle\cdot\rangle_\tau$ denotes the expectation value taken in the time-dependent state. The external bias – an onsite potential $\pm\Delta V n_i$ applied to the leads – is $\Delta V \sim 10^{-3} t$. We use a Trotter-Suzuki break-up of the time evolution operator in our adaptive tDMRG scheme with a time step of $\delta\tau \sim 0.05$ [71,72]. The discarded weight during the time evolution is kept below 10^{-10}. For the tDMRG data to be discussed in Section 3.1, $M \lesssim 800$ states needed to be kept to meet this requirement. With this choice of tDMRG parameters, the real-time data obtained with a discarded weight of 10^{-10} and 5×10^{-10} turn out to be indistinguishable from each other on the scale of the plots. Open boundary conditions are imposed in all DMRG calculations. As for the notation adopted throughout the manuscript, for our DMRG results, $\langle\cdot\rangle$ denotes the expectation value taken in the ground-state calculated with the method in a subspace given by a fixed total number of electrons and a fixed value of $S^z_{\rm total}$. Further note that on chains with an odd number of sites and at half filling, the results on static properties and real-time currents to be presented in the following sections do not depend on whether we work at $S^z_{\rm total} = 1/2$ or $S^z_{\rm total} = -1/2$, with the trivial exception of $\langle S^z_i\rangle$, which changes its sign. For N odd, we hence work in the $S^z_{\rm total} = 1/2$ subspace only.

2.2 ECA

The ECA method relies on the numerical determination of the ground-state of a cluster with open boundary conditions. In the following, we briefly sketch details of the method.

The ECA method tackles the impurity problem in three steps. First, the infinite system is artificially cut into two parts: one part **C** that contains the interacting region plus as many noninteracting sites of the leads as possible (this part will, from now on, be referred to as 'the cluster'), and a second part **R** (the 'rest'), consisting of semi-infinite chains positioned at the left and the right in relation to the cluster **C**. The number of sites in **C** is denoted by N_{ED}. Second, Green's functions (GF) for both parts are computed independently: current implementations of ECA utilize the Lanczos method to calculate the interacting region's GF, while those of the part **R**, being noninteracting, can be computed exactly as well. In a final step, the artificially disconnected parts are reconnected by means of a Dyson equation, which dresses the interacting region's GF. This step, the actual embedding, is crucial for capturing the many-body physics associated with the Kondo effect. Moreover, although the clusters that can be solved exactly by means of a Lanczos routine are rather small, being of the order of $N_{\mathrm{ED}} \approx 12$ sites only, the embedding step largely compensates for that by dressing the cluster GF and effectively extending the many-body correlations, induced by the presence of the impurity, into the semi-infinite chains **R**.

We now further detail these steps. The Hamiltonians of the left and right semi-infinite, tight-binding chains, i.e., the noninteracting **R** part, are described by

$$H_{\mathrm{sc-L}} = -t \sum_{l=0,\sigma}^{-\infty} \left(c_{l\sigma}^{\dagger} c_{l-1\sigma} + \mathrm{h.c.} \right)$$

$$H_{\mathrm{sc-R}} = -t \sum_{l=N_{\mathrm{ED}}+1,\sigma}^{\infty} \left(c_{l\sigma}^{\dagger} c_{l+1\sigma} + \mathrm{h.c.} \right), \qquad (5)$$

where in this notation, the sites labeled by $i = 1, \ldots, N_{\mathrm{ED}}$ are inside the cluster **C**. The semi-infinite chains are connected to the cluster by the following term:

$$H_{\mathrm{rest}} = -V \left[c_{1\sigma}^{\dagger} c_{0\sigma} + c_{N_{\mathrm{ED}}\sigma}^{\dagger} c_{N_{\mathrm{ED}}+1\sigma} \right] + \mathrm{h.c.}, \qquad (6)$$

where $V = t$ is the hopping in the broken link, connecting parts **R** and **C**, used for the embedding procedure. The GF for the cluster **C** and for the semi-infinite chains are calculated at zero temperature. Fixing the number of particles m and the z-axis projection of the total spin, S^z_{total}, the ground state and the one-body propagators between all the clusters' sites are calculated. For example, $g_{ij}^{(m,S^z_{\mathrm{total}})}$, the undressed Green function for the cluster, propagates a particle between sites i and j inside the cluster. For the noninteracting, semi-infinite chains, the GFs g_0^L and $g^R_{N_{\mathrm{ED}}+1}$ at the sites 0 and $N_{\mathrm{ED}}+1$, located at the extreme ends of the semi-infinite chains, at left and right to the cluster, can be easily calculated as well.

The Dyson equation to calculate the dressed GF matrix elements $G_{i,j}^{(m,S^z_{\mathrm{total}})}$ can therefore be written as

$$G_{i,j}^{(m,S^z_{\mathrm{total}})} = g_{i,j}^{(m,S^z_{\mathrm{total}})} + g_{i,1}^{(m,S^z_{\mathrm{total}})}\ V\ G_{0,j}^{(m,S^z_{\mathrm{total}})} + g_{i,N_{\mathrm{ED}}}^{(m,S^z_{\mathrm{total}})}\ V\ G_{N_{\mathrm{ED}}+1,j}^{(m,S^z_{\mathrm{total}})} \qquad (7)$$

with

$$G_{0,j}^{(m,S^z_{\mathrm{total}})} = g_0^L\ V\ G_{1,j}^{(m,S^z_{\mathrm{total}})} \qquad (8a)$$

$$G_{N_{\mathrm{ED}}+1,j}^{(m,S^z_{\mathrm{total}})} = g^R_{N_{\mathrm{ED}}+1}\ V\ G_{N_{\mathrm{ED}},j}^{(m,S^z_{\mathrm{total}})}\ , \qquad (8b)$$

where V, as mentioned above, is defined according to H_{rest}, equation (6). Equations (7) and (8) correspond to a chain approximation, where a locator-propagator diagrammatic expansion is used [73,74]. Note that ECA is exact in the case of $U = 0$.

As mentioned before, the calculation of the propagator $g_{i,j}^{(m,S^z_{\mathrm{total}})}$ requires that fixed quantum numbers m and S^z_{total} be used. However, after the embedding procedure, these quantum numbers are not good quantum numbers for the cluster anymore. Therefore, we have to incorporate processes into the ECA method that allow for charge fluctuations in the cluster **C**. To accommodate this requirement, different implementations of ECA have been devised, either by including different spin-mixing strategies [25,47,75,76] or by moving the Fermi energy of the leads [77,78].

For this work, we will adopt a spin-mixing strategy different from the one used in a previous work analyzing the three-dots geometry [28]. We will show that this different strategy is instrumental in decreasing finite-size effects observed in reference [28]. The spin mixing proceeds as follows. First, a cluster GF with mixed charge is defined through

$$g_{i,j}^{(m+p,pS^z_{\mathrm{total}})} = (1-p)\ g_{i,j}^{(m,0)}\ +\ p\ g_{i,j}^{(m+1,S^z_{\mathrm{total}})}, \qquad (9)$$

where p takes values between 0 and 1, and we assume that m is even, in which case, the corresponding $S^z_{\mathrm{total}} = 0$. In addition, note that for the cluster with charge $m+1$, S^z_{total} takes values $\pm 1/2$. The matrix element $g_{i,j}^{(m+p,pS^z_{\mathrm{total}})}$ corresponds to a situation where the charge in the cluster is between m and $m+1$. The total charge in the cluster, before embedding, can be easily calculated as

$$q^{pS^z_{\mathrm{total}}}(p) = (1-p)m + p(m+1) = m + p. \qquad (10)$$

Using equations (7) and (8), the dressed GF $G_{i,j}^{(m+p,pS^z_{\mathrm{total}})}$ is obtained, and from this result, the charge in the cluster can be calculated:

$$Q^{pS^z_{\mathrm{total}}}(p) = \frac{-1}{\pi} \int_{-\infty}^{E_F} \mathrm{Im} \left\{ \sum_i G_{i,i}^{(m+p,pS^z_{\mathrm{total}})}(\omega) \right\} d\omega, \qquad (11)$$

where E_F is the Fermi level. The value of p is calculated self-consistently, satisfying

$$Q^{pS^z_{\mathrm{total}}}(p) = q^{pS^z_{\mathrm{total}}}(p). \qquad (12)$$

If there is spin reversal symmetry, e.g., no magnetic field is applied, one can calculate the total GF as

$$G_{i,j}(p) = \frac{1}{2} \sum_{S^z_{\rm total}=\pm 1/2} G_{i,j}^{(m+p,pS^z_{\rm total})}, \qquad (13)$$

where p satisfies equation (12). It is important to emphasize that the charge fluctuations taken into account by equation (9) are the ones between the cluster and the rest of the system, and not just the ones at the interacting region described by $H_{\rm int}$. The latter ones involve a very localized neighborhood of the dot and as a consequence, are typically already well described on isolated clusters only.

As will be shown in Section 4.2, this alternative way of obtaining the dressed GF leads to improved results in the case of three dots. Note that in the case of one dot, no substantial difference in the final results obtained from either the old spin-mixing strategy [25,47,75,76] or the one described here is found. Yet, for the sake of consistency, we apply the same way of spin mixing as described here throughout the paper.

It is noteworthy to point out that the self-consistent solution for the charge-mixing parameter p is either 0 or 1 in the Kondo regime. Therefore, in the Kondo regime, where charge fluctuations are suppressed, no charge mixing is done at all. The parameter p takes a finite value $0 < p < 1$ as the gate potential drives the system into the mixed-valence regime, and the purpose of the charge mixing is thus mainly to smoothen out the transition from an m electron to an $m \pm 1$ electron ground state, that for the bare cluster would be a discontinuous one. From a conceptual point of view, the introduction of the parameter p establishes a necessary consistency in the theory guaranteeing that the number of electrons in the cluster is the same before and after the embedding process.

For completeness, we give the actual expression that we compute the conductance G from [25,26,79]:

$$G = G_0 \left[t^2 \rho_{\rm leads}(E_F)\right]^2 |G_{l,r}(E_F)|^2 \qquad (14)$$

here, $\rho_{\rm leads}(E_F)$ is the density of states of the leads at the Fermi-level E_F and $G_{l,r}(\omega)$ is the dressed Green function that propagates an electron from the first site l left of the cluster to the first site right r of the cluster.

3 Transport through a single quantum dot revisited

In this section, we focus on the application of tDMRG and ECA to the study of the conductance of a single quantum dot. The interacting portion of the Hamiltonian (1) is:

$$H_{\rm int} = U n_{{\rm dot},\uparrow} n_{{\rm dot},\downarrow} + V_g n_{\rm dot}, \qquad (15)$$

where the Coulomb repulsion U represents the charging energy, V_g is the gate potential, and $n_{\rm dot} = n_{{\rm dot},\uparrow} + n_{{\rm dot},\downarrow}$ is the dot's charge. The model is particle-hole symmetric at $V_g = -U/2$.

As has been shown in reference [17], tDMRG is capable of producing zero-temperature transport properties of the single-impurity Anderson model for $U/(2t'^2) \lesssim 4$, such as the conductance as a function of gate potential or its dependence with a magnetic field. In that previous work, it was noticed that the behavior of real-time currents on finite systems with open boundary conditions is quite different depending on odd-even effects. When the number of sites in each lead is even or odd, we have a $S^z_{\rm total} = 1/2$ ground-state, while with an odd number of tight-binding sites in one lead and an even number in the other, the system has an overall $S^z_{\rm total} = 0$ ground state. Here we present a detailed scaling analysis of static properties that explains why the latter type of clusters is preferable, as suggested in reference [17].

Finally, we discuss finite-size effects in the context of ECA, which are of similar origin, and we provide a quantitative comparison with exact results obtained through the Friedel sum rule [61] and ground-state DMRG.

3.1 Motivation: tDMRG results

Let us motivate our study by discussing results from tDMRG for the current through a quantum dot at small external biases. On an open chain with one embedded dot, we analyze three configurations: (i) an odd number of sites in both leads (o1o); (ii) an even number of sites in both leads (e1e), (iii) or an overall even number of sites (o1e). We repeat some of the main results obtained in reference [17] for the o1e cluster-type, which has mostly been used in that work. First, both at zero and finite U, the current is almost constant in time over an extended period in time, allowing us to assign a conductance value $G(N) = J(\tau)/\Delta V$ to each chain of finite length. Note that the length in time of such constant current is limited by twice the time that it takes the current to be reflected at the open boundaries. Second, performing a finite-size scaling of $G(N)$, one finds that it extrapolates, following a simple scaling law of the form $G(N) \sim 1/N$, to the known exact results from Fermi liquid relations [61] for $U/2t'^2 \lesssim 4$. Third, e1e clusters have been found to exhibit a slower convergence and generally lower current values. Our discussion in this section will mostly focus on clusters with $S^z_{\rm total} = 1/2$, i.e., e1e and o1o ones.

The behavior of a current driven by a small bias is illustrated in Figure 2 for clusters of an intermediate length and at half filling. It is important to notice that we choose values for U and t' as well as cluster sizes such that the finite-size effect we wish to address is clearly visible. As a drawback, obviously, a steady state with $G \sim G_0$ is not reached for the three clusters and system sizes considered in Figure 2. Longer chains are needed for this set of U and t' since (i) finite-level spacings possibly cut off the Kondo resonance and (ii) the time-scale for reaching the steady state [80,81] may exceed the time at which the current reverses its sign.

We now turn to this section's main point, the discussion of even-odd effects in the current. e1e clusters result in the smallest current, o1e clusters yield a larger current

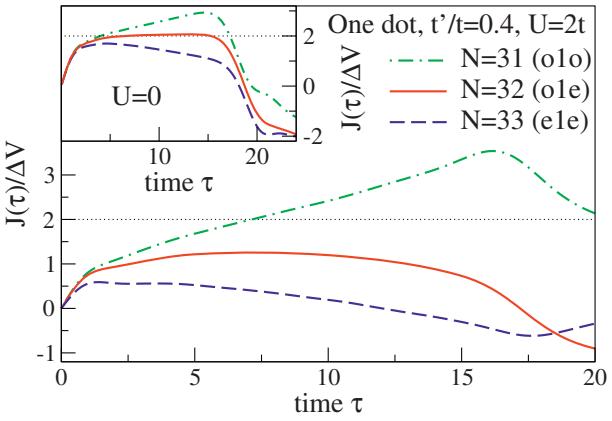

Fig. 2. (Color online) One dot, $t'/t = 0.4$, $V_g = -U/2$. Main panel: current $J(\tau)/\Delta V$ vs. time for $N = 31$ (o1o), $N = 32$ (o1e), and $N = 33$ (e1e) at $U/t = 2$ (tDMRG). Inset: current $J(\tau)/\Delta V$ vs. time at $U = 0$ for $N = 31, 32, 33$ (exact diagonalization). We divide $J(\tau)$ by the bias ($\Delta V = 10^{-3}t$). Perfect conductance corresponds to $J(\tau)/\Delta V = 2$ (indicated by horizontal, dotted lines).

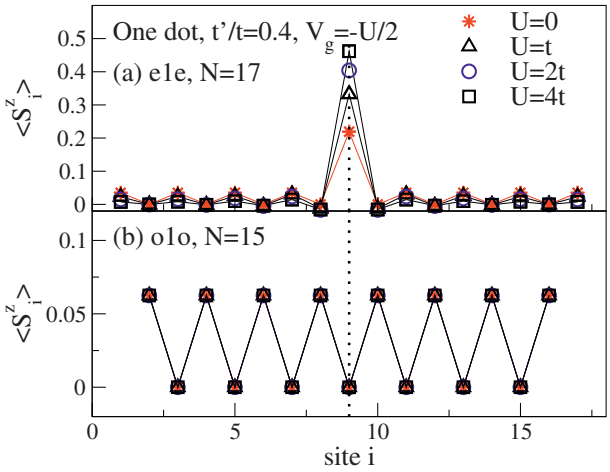

Fig. 3. (Color online) One dot, $t'/t = 0.4$, $V_g = -U/2$. Spin density $\langle S_i^z \rangle$, for (a) $N = 17$ sites (e1e) and (b) $N = 15$ sites (o1o) with $U/t = 0, 1, 2, 4$. (a) Even at $U = 0$, the z-component of the total spin is essentially carried by the central site, i.e., the dot. (b) In the o1o case, overall, every second site carries a positive $\langle S_i^z \rangle$. The dotted vertical lines denote the position of the dot. DMRG data with $M = 300$. The results presented here for o1o and e1e agree with reference [62]. DMRG calculations are all performed in subspaces with a fixed number of fermions and $S^z_{\rm total}$, and the symbol $\langle \cdot \rangle$, here and throughout, refers to taking the expectation value in the ground state of such subspaces.

and exhibit the aforementioned behavior of being approximately constant in time ($J(\tau) \approx$ const.) before the reversal of the current's sign occurs, o1o clusters allow for a substantially larger current that even exceeds – if considering the conductance $G = J/\Delta V$ – perfect conductance $G_0 = 2$, but that is never constant in time. These differences are quite striking, considering that the system sizes used in Figure 2 differ by only one site in the leads. It is worth pointing out that these strong finite-size effects are in principle not caused by the presence of the Coulomb repulsion on the dot, but can even be seen in the noninteracting case $U = 0$, as displayed in the inset of Figure 2. Note that when the system size is increased, $J(\tau)/\Delta V$ measured on o1o clusters approaches perfect conductance from above. We stress that the strong differences in $J(\tau)$ depending on the cluster type are not due to current-ringing [80,81], which is most pronounced away from half filling ($V_g \neq -U/2$) or at large biases [18,71,82].

The crucial difference between o1e on the one hand and the other two clusters on the other hand is the finite magnetic moment $S^z_{\rm total} = 1/2$ present in the system in the case of an overall odd number of sites. As we shall see, this finite moment is not homogeneously distributed over the system. Let us first explain the suppressed conductance seen in the case of the e1e clusters. Figure 3a shows the local spin density $\langle S_i^z \rangle$ for $N = 17$ sites and several values of $U/t = 0, 1, 2, 4$. Clearly, for any U, most of the $S^z_{\rm total}$ is carried by the central site, i.e., the quantum dot [62]. The reason for this inhomogeneous distribution is easy to understand, considering the critical tendency of 1D systems towards antiferromagnetic (AFM) correlations at half filling. For that reason, the spin cannot be homogeneously distributed over all sites. We further observe that on open systems, the spins on the first and last tight-binding site point up, which then, with an even number of sites to the left and right of the dot, favors the spin on the dot to point up as well. In other words, both leads form an approximate singlet, leaving the remaining moment $S^z_{\rm total}$ on the dot. This is strictly true in the limit of $t' = 0$, where $\langle S^z_{\rm dot} \rangle = 1/2$, while each lead has a vanishing $\langle S^z_{\rm total} \rangle$. Increasing t' then reduces $\langle S^z_{\rm dot} \rangle$. Upon increasing U at a fixed $t' > 0$, a larger fraction of $S^z_{\rm total}$ is pinned at the dot site, as charge fluctuations that tend to reduce the local moment are suppressed by increasing U.

Qualitatively, the situation of an e1e cluster is equivalent to a quantum dot in the presence of a magnetic field: locally, the Z_2 symmetry $S^z_{\rm dot} \leftrightarrow -S^z_{\rm dot}$ is broken on e1e clusters. A magnetic field is well-known to split the Kondo resonance thus leading to a reduced conductance [61]. In order to support this picture, we use e1e clusters and apply a *real* magnetic field onto the dot:

$$H_{\rm field} = h_{\rm dot} S^z_{\rm dot}; \quad S^z_{\rm dot} = \frac{1}{2}\left(n_{{\rm dot},\uparrow} - n_{{\rm dot},\downarrow}\right). \qquad (16)$$

As expected, when $\langle S^z_{\rm dot} \rangle$ decreases upon applying the field $h_{\rm dot}$ – as now the field favors a *negative* spin in the dot – the current increases, as we show in Figure 4. For the parameters of Figure 4 ($N = 33$, e1e) we infer from the figure's inset that the spin projection on the dot vanishes at about $h_{\rm dot} \approx 0.34t$. Consistently, the current measured in tDMRG simulations at $h_{\rm dot} \approx 0.35t$ reaches values similar to those observed using o1o clusters of comparable system size. This establishes a connection between the dot's polarization and the achievable currents. Note further that e1e clusters behave exactly like o1o ones if the filling is kept at $(N \pm 1)/N$ (not shown).

Finally, note that the finite spin projection in the cluster's ground-state is an issue of parameters. Increasing the

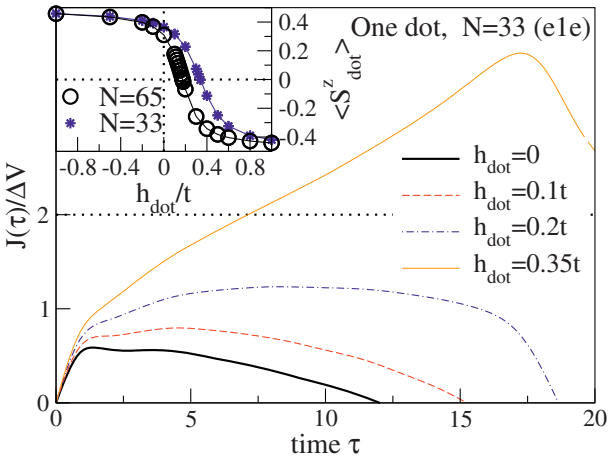

Fig. 4. (Color online) One dot, $t'/t = 0.4$, $U/t = 2$, $V_g = -U/2$. Main panel: tDMRG data for the current $J(\tau)/\Delta V$ vs. time for $N = 33$ and several values for a magnetic field $h_{\rm dot}$ applied to the dot: $h_{\rm dot}/t = 0$, 0.1, 0.2, 0.35 (see Eq. (16)). The inset shows $\langle S^z_{\rm dot}\rangle$ as a function of $h_{\rm dot}$ for $N = 33$ and 65, calculated with ground-state DMRG ($M = 300$).

coupling to the leads, i.e., t', at fixed U and system size (say, $N = 33$, e1e), delocalizes the spin and a larger current is then measured in tDMRG calculations.

For the second type of clusters with a nonzero $S^z_{\rm total}$, o1o, we find that the spin is equally distributed over every second site [62], displayed in Figure 3b. Since the out-most sites carry a positive $\langle S^z_i\rangle > 0$, the dot now has a nearly vanishing $\langle S^z_{\rm dot}\rangle$. Consistent with the notion of $\langle S^z_{\rm dot}\rangle \approx 0$, the spin projections on the dot and all other sites are practically independent of the Coulomb repulsion U.

It is important to stress that at fixed odd N, both types of behavior can be produced: when shifting the dot in a $N = 33$ cluster by one site, a 17-dot-15 configuration is obtained. The current now behaves almost exactly like the one measured on an $N = 31$ (o1o, 15-dot-15) cluster and so does the z-component of the spin. The same holds for an asymmetric $N = 31$ cluster with a 16-dot-14 configuration: the dot now carries most of the $S^z_{\rm total}$ and the current is suppressed, similar to the case of $N = 33$ (16-dot-16, e1e). The corresponding DMRG results are not shown in the figures, but are quantitatively similar to Figures 2 and 3. These considerations show that indeed the distribution of $S^z_{\rm total}$, which depends on the geometry and model parameters, affects the conductance.

We finally emphasize that the issue of a non-uniformly distributed $\langle S^z_i\rangle$ on half-filled chains with an odd number of sites and constant hopping matrix elements in the leads also emerges in other interacting systems that do not feature Kondo physics, such as transport through a Mott insulator or an even number of quantum dots [83]. Its influence on the finite-size scaling of transport properties is most significant in Kondo problems, though.

3.2 Static properties: gate potential dependence

To render the line of reasoning outlined in Section 3.1 more quantitative we proceed with a systematic discussion of static properties that are crucial to characterize a dot in the Kondo regime: spin and charge fluctuations on the dot, as well as spin-spin correlations between the dot and the leads. For this purpose, we focus on the parameter set $t'/t = 0.4$ and $U/t = 4$ and the dependence on the gate potential, keeping the full system at half filling.

First of all, let us recall some of the hallmark features of the single-impurity Anderson model at $T = 0$ [13,61]: (i) a slowly varying charge $\langle n_{\rm dot}\rangle \approx 1$ on the dot in a broad gate-potential window $-1 \lesssim V_g/U \lesssim 0$ for $\Gamma \ll U$, where Γ denotes the hybridization parameter. This property, i.e., the almost constant charge, becomes more pronounced as U/Γ increases; (ii) enhanced spin fluctuations on the dot; (iii) large charge fluctuations at the charge degeneracy points $V_g/U = -1, 0$, but a suppression of charge fluctuations in between. While the spin fluctuations at the particle-hole symmetric point increase with increasing U/Γ, the charge fluctuations decrease at the same time. Still, the conductance is always perfect, since the scattering of conduction electrons screens the magnetic moment, giving rise to the large spin fluctuations. We characterize charge and spin fluctuations via:

$$(\delta S^z_{\rm dot})^2 = \langle (S^z_{\rm dot})^2\rangle - \langle S^z_{\rm dot}\rangle^2; \tag{17}$$

$$(\delta n_i)^2 = \langle n_i^2\rangle - \langle n_i\rangle^2. \tag{18}$$

Properties (ii) and (iii) of the single-impurity Anderson model can nicely be seen in Figures 5a and 5b: o1o and o1e clusters exhibit a broad maximum in the spin fluctuations around the particle-hole symmetric point $V_g = -U/2$, while charge fluctuations are suppressed (Figs. 5a and 5b). The maxima in $(\delta n_{\rm dot})^2$ vs. V_g/U at $V_g/U = -1, 0$ are due to the charge degeneracy between states with $n_{\rm dot} = 0$ and 1 and $n_{\rm dot} = 1$ and 2, respectively. For comparison, DMRG results for $N = 200$ sites (triangles) are included in Figures 5a and 5b.

As for the e1e clusters, we emphasize that the main consequence of the finite spin projection $\langle S^z_{\rm dot}\rangle$ present for $-1 \lesssim V_g/U \lesssim 0$ (see Fig. 5c) on the dot is a reduction of spin fluctuations (see Fig. 5b). A Kondo-resonance, however, which is at the heart of perfect transmission through a quantum dot at the particle-hole symmetric point, emerges as a consequence of virtual charge fluctuations due to scattering of conduction electrons off the impurity that cause substantial spin fluctuations on the dot, thus screening its moment [61].

Apart from spin fluctuations, and equally importantly, spin-spin correlations between the dot and the leads are affected as well. Figure 5d shows the spin-spin correlations between the dot and the first site in the leads:

$$S^z_{ij} = \langle S^z_i S^z_j\rangle - \langle S^z_i\rangle\langle S^z_j\rangle, \tag{19}$$

which are substantially smaller around the particle-hole symmetric point $V_g = -U/2$ on e1e clusters than for other clusters. These two features illustrate the failure of e1e clusters to harbor precursors of Kondo physics as long as system sizes are small. We shall discuss the finite-size scaling below.

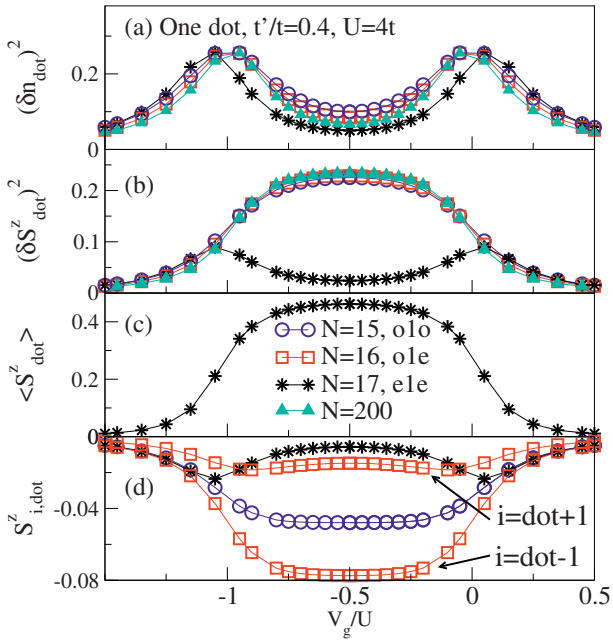

Fig. 5. (Color online) One dot, static properties computed with DMRG as a function of gate potential V_g/U at $t'/t = 0.4$, $U/t = 4$, comparing different cluster types: o1o ($N = 15$, circles), o1e ($N = 16$, squares), and e1e ($N = 17$, stars). Triangles in (a) and (b) are for a large system of $N = 200$ sites ($M = 300$ DMRG states). (a) Charge fluctuations $(\delta n_{\rm dot})^2$; (b) spin fluctuations $(\delta S^z_{\rm dot})^2$; (c) local spin density $\langle S^z_{\rm dot}\rangle$ on the dot; and (d) spin-spin correlations $S^z_{i,\rm dot}$ between the dot and the first neighboring site in the leads. For o1e clusters such as $N = 16$, there is an asymmetry between the left and the right lead: the dot is mostly screened by the left lead, i.e., the one that has an odd number of sites.

Let us next discuss how the emergence of screening is reflected in the spatial extension of spin-spin correlations. DMRG results for spin-spin correlations (see Eq. (19)), measured away from the dot, and for their integral $S_z(r)$,

$$S_z(r) = \sum_{\substack{i \text{ with} \\ r'(i)\le r}} S^z_{i,i_{\rm dot}}, \quad r'(i) = |i - i_{\rm dot}|, \qquad (20)$$

are displayed in Figures 6a and 6b, respectively, for $N = 31$ (o1o), $N = 32$ (o1e), and $N = 33$ (e1e). We first observe from Figure 6a that, while the leads are symmetrically polarized in the case of $N = 31$, o1e clusters mainly polarize one lead, namely the one that has an odd number of tight-binding sites. In this case, an *approximate* singlet is formed with this lead. When integrated over distance, the spin correlations behave quite similarly for these two cluster types, i.e., o1e and o1o. In contrast to that and consistent with the notion of the absence of Kondo physics on small e1e clusters, only small spin-spin correlations spread out into the leads for these clusters.

3.3 Static properties: finite-size scaling

We proceed by discussing the finite-size scaling of static properties. Our DMRG results for system sizes

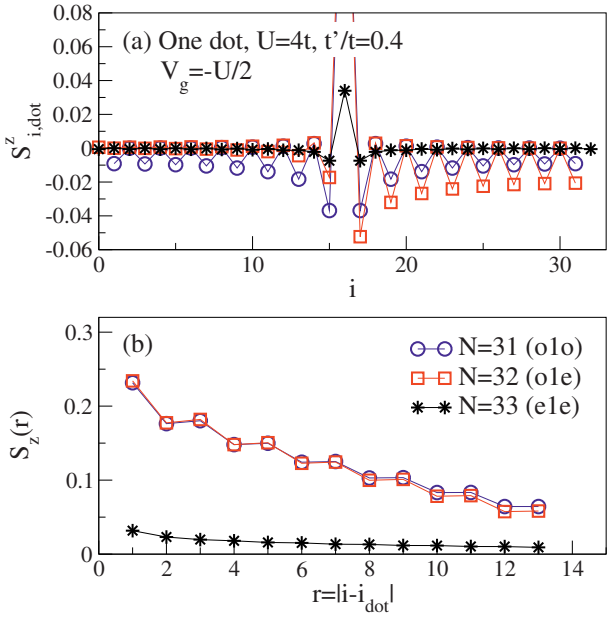

Fig. 6. (Color online) One dot, $t'/t = 0.4$, $U/t = 4$, $V_g = -U/2$. (a) Spin-spin correlations vs. site, (b) integrated spin-spin correlations $S_z(r)$ (see Eq. (20)) vs. distance r. DMRG data are shown for $N = 31$ (circles, o1o), $N = 32$ (squares, o1e), $N = 33$ (stars, e1e); $M = 300$. See the text in Section 3.2 for a discussion.

$15 \le N \le 400$ are displayed in Figure 7. The main observations are:

(i) spin and charge fluctuations converge the fastest on o1e clusters;
(ii) in the case of e1e, the dot carries a large, finite $\langle S^z_{\rm dot}\rangle$ that decays slowly with N, suppressing spin fluctuations and spin-spin correlations with the dot's neighboring sites;
(iii) antiferromagnetic spin-spin correlations $S^z_{i,\rm dot}$ are enhanced in the case of o1o clusters on small systems, while on o1e clusters, mainly the lead with an odd number of sites develops substantial AFM correlations with the dot.

3.4 ECA results for the conductance

Early studies [27] using this technique have phenomenologically proposed that for one dot, the best results are obtained when it is neighbored by an odd number of sites (o1o), while e1e clusters exhibit a Coulomb-blockade like behavior. Using insights of Sections 3.2 and 3.3, we can now explain this observation on a more rigorous basis. Small e1e clusters typically locate the $S^z_{\rm total} = 1/2$ to a large extent onto the quantum dot, thus giving rise to a split resonance. Consistently, we find a charge gap in the local density of states (LDOS). While the embedding procedure manages to redistribute spectral weight in the LDOS quite well [84], it does not close the charge gap given by the exactly solved interacting region.

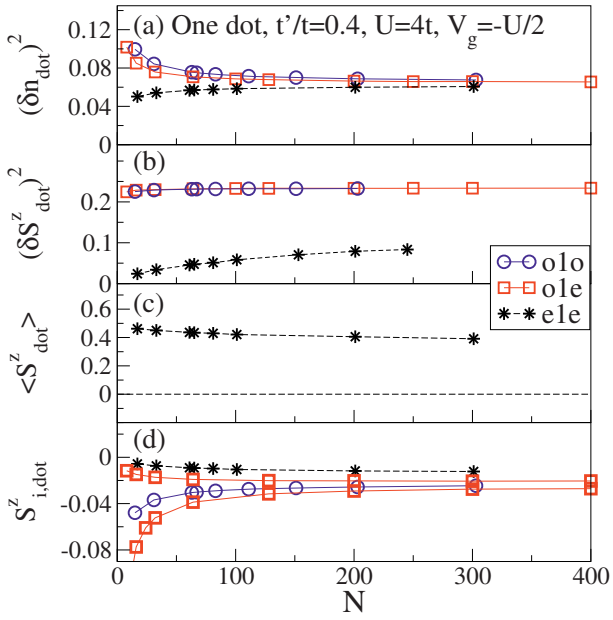

Fig. 7. (Color online) One dot, $t'/t = 0.4$, $U/t = 4$, $V_g = -U/2$. Finite-size scaling analysis of static properties: (a) charge fluctuations on the dot; (b) spin fluctuations on the dot; (c) local spin $\langle S^z_{\rm dot}\rangle$ on the dot (compare Ref. [62]); (d) spin-spin correlations between the dot and its neighboring sites. In (d), the upper o1e curve is for i in the right lead (i = dot + 1), while the lower one is for i in the left lead (i = dot − 1). DMRG results ($M \leq 500$) are shown for o1o (circles), o1e (squares), and e1e clusters (stars).

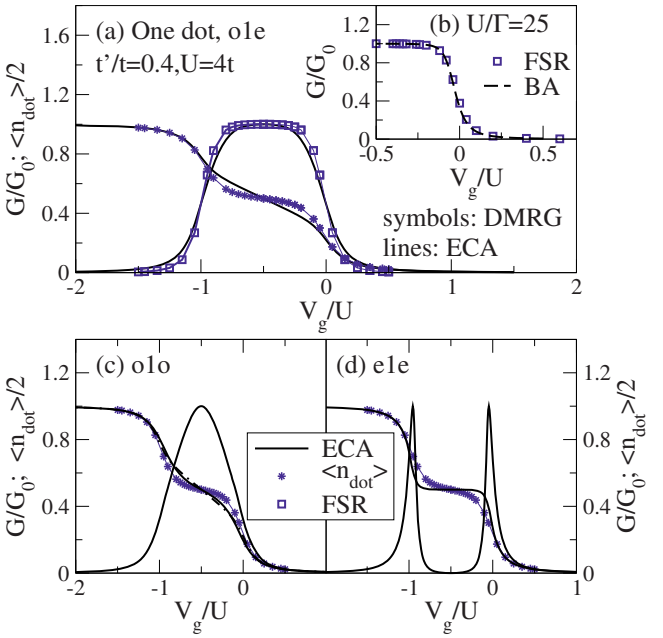

Fig. 8. (Color online) One dot, $t'/t = 0.4$, $U/t = 4$. (a) Conductance G and charge $\langle n_{\rm dot}\rangle$ vs. gate potential V_g/U for o1e (ECA, $N_{\rm ED} = 12$, solid lines), and DMRG results for the charge and G obtained through the FSR (circles and squares, respectively). ECA results for an 1o cluster with $N_{\rm ED} = 10$ sites are indistinguishable from the o1e curve. (b) Comparison of conductance obtained from the Friedel sum rule using DMRG data for the charge $\langle n_{\rm dot}\rangle$ ($N = 300$, $M = 500$, $U/t = 0.5$, $t'/t = 0.1$) with Bethe-ansatz results from reference [60]. (c) Conductance G and charge $\langle n_{\rm dot}\rangle$ vs. gate potential V_g/U for o1o (ECA, $N_{\rm ED} = 11$, solid lines), and DMRG results for the charge (circles). (d) Conductance G and charge $\langle n_{\rm dot}\rangle$ vs. gate potential V_g/U for e1e (ECA, $N_{\rm ED} = 9$, solid lines), and DMRG results for the charge (circles).

For illustration, we show ECA results for one dot at $t'/t = 0.4$, $U/t = 4$ and all three cluster types in Figures 8a, 8c, and 8d. The conductance is computed from equation (14). The figure also contains the conductance as obtained from the Friedel sum rule (FSR) using the charge computed with static DMRG [61]:

$$G = G_0 \sin^2(\pi\langle n_{\rm dot}\rangle/2), \tag{21}$$

where $G_0 = 2$ due to spin degeneracy. Here we claim that the charge $\langle n_{\rm dot}\rangle$ can be obtained to high precision from ground-state DMRG. To support this we show a comparison for the conductance derived from equation (21) with exact Bethe-ansatz results [60] in Figure 8b for $U/\Gamma = 25$. Note that in the wide-band limit $U < 4t$, the hybridization parameter is $\Gamma = 2\pi t'^2\rho_{\rm lead}$, and since we work with semi-infinite-leads, $\rho_{\rm lead} = 1/(\pi\, t)$ [79]. Our DMRG results are for $U = 0.5t$, $t'/t = 0.1$. We find excellent agreement with the results from reference [60] in the limit of a large U/Γ, which justifies the use of static DMRG to benchmark the ECA results at smaller values of $U/\Gamma \sim 12$.

Clearly, the o1e clusters are closest to the FSR as shown in the main panel of Figure 8a. In Figure 8d, we further observe a Coulomb blockade type-of behavior for e1e clusters. Regarding the o1o cluster, although it qualitatively provides the correct physical description, the conductance plateau comes out too narrow as the charge around the particle-hole symmetric point $V_g = -U/2$ varies too fast as compared to the DMRG result (see Fig. 8c). Note that the ECA results for the charge $\langle n_{\rm dot}\rangle$ as displayed in Figure 8 are obtained *after* embedding by integrating over the imaginary part of the dot's onsite Green's function.

A further improvement of results can be achieved by using a transformation onto bonding and anti-bonding orbitals in the Hamiltonian for one dot, equations (1)–(3), and (15) (see, e.g., Refs. [10,11] and references therein):

$$b^\dagger_{i,\sigma} = \frac{1}{\sqrt{2}}\left[c^\dagger_{i_L,\sigma} + c^\dagger_{i_R,\sigma}\right], \quad a^\dagger_{i,\sigma} = \frac{1}{\sqrt{2}}\left[c^\dagger_{i_L,\sigma} - c^\dagger_{i_R,\sigma}\right] \tag{22}$$

here, the index i measures the distance away from the dot and i_L, i_R are the corresponding indices in the two semi-infinite leads. The transformation decouples the dot from the anti-bonding states, leaving it coupled only to the bonding states. This is technically a great simplification as leads almost twice as large can now be treated. While such transformation cannot be used for the spatially asymmetric o1e clusters, it works for e1e and o1o. We observe that exactly the same result is found for e1e, comparing, say, the full $N = 9 = 4$-dot-4 with the symmetrized dot-4 clusters. Here, the spin still cannot be screened in a singlet

state. For o1o, the results substantially improve, as now, effectively a dot-odd (1o) cluster is solved that has an overall $S^z_{\rm total} = 0$ ground-state, allowing for singlet formation. This gives results similar to those obtained from an o1e configuration with less computational effort, as a smaller cluster is diagonalized.

Our observations lend strong support to the idea that when the global quantum numbers of the exactly solved cluster allow for a singlet state to be the ground state – as is the case for o1e and 1o clusters – then a precursor of the Kondo effect can be seen even on small ED clusters, with a favorably fast convergence with system size.

Finally, Figures 8a, 8c, and 8d suggest a way to gauge the quality of ECA data even in a situation where no exact results for the conductance are available. We see that the cluster type that produces the best charge vs. gate potential curve yields the best G vs. V_g curve as well. Thus, performing a finite-size scaling analysis of properties such as the charge or spin fluctuations using either a Lanczos routine (which is a part of standard ECA codes, see Sect. 2.2) or DMRG is well suited to identify the *optimum* cluster type to be used in conductance calculations in ECA.

3.5 One quantum dot: summary

Let us summarize our observations from this Section 3. We can understand the behavior of reflection-symmetric clusters with an odd number of sites and an $S^z_{\rm total} = 1/2$ ground state in terms of rigid spins $\langle S^z_i \rangle$ pinned to certain sites. In the case of e1e, the dot is mostly polarized and carries a finite magnetization. This is qualitatively equivalent to the application of a magnetic field that causes Zeeman splitting of the Kondo resonance and, thus, a suppression of the conductance [61]. For the case of o1o clusters, the leads are polarized, with only every second site carrying a finite magnetization [62]. For comparable system sizes, a substantially larger current is observed on these clusters, which, in tDMRG simulations, however, does not exhibit a current that is constant in time for $t' \neq t$.

Our analysis further suggests that either o1e or 1o clusters are best suited to study the emergence of Kondo physics with techniques such as tDMRG or ECA, while on system sizes accessible to these techniques, e1e clusters yield qualitatively different results with essentially a Coulomb-blockade like behavior. The overall conclusion is that in order to provide a reliable description of the many-body effects at the Fermi level, clusters with a $S^z_{\rm total} = 0$ ground state are necessary in calculations with these two methods. Among these, the advantage of 1o clusters is that larger system sizes can be accessed. Finally, we stress that no matter what the cluster type is, if one was able to go to extremely long chains, the same physics would be recovered [62].

4 Three dots

We now turn to a more complicated case, three serially coupled dots, as shown in Figure 1b. Apart from the interest in the emergence of Kondo physics, many quantum dots arranged in an array can be considered an interpolation between a single localized impurity and a bulk Mott insulator. In the first case, the transmission at half filling is perfect, but zero in the later due to the presence of the Mott gap [85].

The interacting region is described by

$$H_{\rm int} = -t'' \sum_{i=1}^{2} \left(c^\dagger_{i,\sigma} c_{i+1,\sigma} + \text{h.c.} \right) + U \sum_{i=1}^{3} n_{i,\uparrow} n_{i,\downarrow} + \sum_{i=1}^{3} V_g n_i. \quad (23)$$

To simplify the notation, we will refer to the dots as **D1**, **D2**, and **D3**, where **D2** is the central dot. We focus on the behavior at the particle-hole symmetric point unless stated otherwise. In the case of three dots, we distinguish between odd-3-odd (o3o), odd-3-even (o3e), and even-3 even (e3e) clusters.

Following references [40,67], for large $t'' \gtrsim U/\sqrt{2}$, the three dots can be viewed as a molecule with, at half filling, two electrons occupying its lowest state, and a resulting $S^z_{\rm total} = 1/2$ from the third electron. For intermediate $t'' \sim 0.3U$, it has been suggested that the three dots behave as a linear antiferromagnet due to strong AFM spin-spin correlations between them. Finally, at small $t'' \ll U$, the system enters a very subtle two-stage Kondo regime. First, and below a Kondo scale $T_K^{(1)}$, the outer dots form a Kondo singlet with their adjacent leads. Then, at temperatures below a second Kondo scale $T < T_K^{(2)} < T_K^{(1)}$, the central dot is screened by the quasi-particles of the two Fermi liquids formed by the outer dots and their leads. Although $T_K^{(2)}$ is orders of magnitude smaller than $T_K^{(1)}$ [40,86], which renders an experimental confirmation of the effect a challenging task, nevertheless the two-stage process conceptually plays an important role for extremely low temperature physics. In all three cases and at temperature $T = 0$, the system possesses a spin $S = 1/2$ Kondo ground state.

Concerning the issue of the conductance, several studies using a variety of approaches such as perturbation theory [65], NRG [67,68], and functional renormalization group [36] report perfect conductance at the particle-hole symmetric point due to the Kondo effect. An earlier ECA work on this model [28] is at odds with this conclusion. In particular, an exact zero of the conductance at the particle-hole symmetric point has been found for all values of t'' studied, i.e., $t'' \lesssim 0.5t$.

We show that the vanishing of G at $V_g = -U/2$ at $t''/t \lesssim 0.3$ is due to the choice of o3o clusters for the ECA calculations of reference [28]. At large $t'' > t'$, this dip is an artefact of certain approximations taken in the embedding procedure: if we perform the ECA according to the prescription of Section 2.2 without mixing Green functions for spin up and and down before the embedding is carried out, this artifact will disappear on o3o clusters.

We shall outline below that the optimum cluster type – in the sense of fastest convergence of static properties

with system size – is o3e. On this cluster type, no spurious dip at $V_g = -U/2$ exists, independent of the spin-mixing strategy adopted in ECA calculations, and the ECA results then are in agreement with the conclusions of references [36,65,67,68].

The section is organized as follows: We first analyze static properties and their finite-size scaling in Section 4.1. Section 4.2 contains our ECA results, obtained following the procedure discussed in Section 2.2, for the conductance. In Section 4.3, we briefly discuss the results one obtains in the regime of $t'' \lesssim t'$ using o3e clusters.

4.1 Static properties: finite-size scaling

Let us first consider the three dots isolated from the leads ($t' = 0$) at $U = t$ as a function of t''/t, which will help to understand e3e and o3o clusters. In the $S^z_{\rm total} = 1/2$ subspace, the two lowest-lying states are both doublets ($S = 1/2$), however, with different spin projections $\langle S^z_i \rangle$ on the dots. The ground state has – schematically – an up-down-up pattern, while the first excited state realizes an up-up-up structure, with most of the $S^z_{\rm total} = 1/2$ on the central dot. The actual distribution of $\langle S^z_i \rangle$ depends on t''/U for a given t', but when the isolated cluster is embedded in leads with an overall odd number of sites (i.e., all sites in the leads plus the three dots), the two low-lying states are mixed with different weights: on o3o clusters, an down-up-down configuration is preferred, while on e3e ones, the original ground-state pattern (up-down-up) prevails. We illustrate this in Figure 9 where we plot $\langle S^z_i \rangle$ vs. t''/t' for $N = 13$ (o3o) and $N = 15$ (e1e). We further see that, as a function of increasing t''/t, the spin projection on the central dot (displayed with stars in the figure) is substantially reduced and moved to the leads in the case of o3o. The large $\langle S^z_i \rangle$ located on the outer dots (displayed with squares in the figure) seen in the case of e3e decays much slower as a function of t''/t.

The rigid spins on either of these cluster types imply suppressed spin fluctuations for the individual dot (**D2** in the case of o3o and **D1**, **D3** in the case of e3e) as well as modified spin-spin correlations. As two case examples, we present the finite-size scaling of such quantities with system size in Figures 10 and 11 for $U = t$, $t'/t = 0.3$ with $t''/t = 0.05$ and $t''/t = 1$.

Let us first discuss e3e clusters (circles in Figs. 10 and 11). Due to the large spin projection on the outer two dots, spin fluctuations as well as the spin-spin correlations with the first site in the leads are suppressed. The latter is an indicator of how strongly the dots polarize the leads. Since the spin-projections $S^z_{\mathbf{D1}}$ and $S^z_{\mathbf{D3}}$ are – both at small and large t'' – only slowly redistributed to other sites as the system size grows, as is evident from Figures 10a and 10c, we conclude that these clusters will produce low conductance values or currents in ECA and tDMRG calculations, respectively.

The o3o clusters (triangles in Figs. 10 and 11) are the ones originally used in reference [28]. Figure 10b reveals that spin fluctuations on the central dot are suppressed in the limit of small $t'' \lesssim t$, which is due to a large fraction

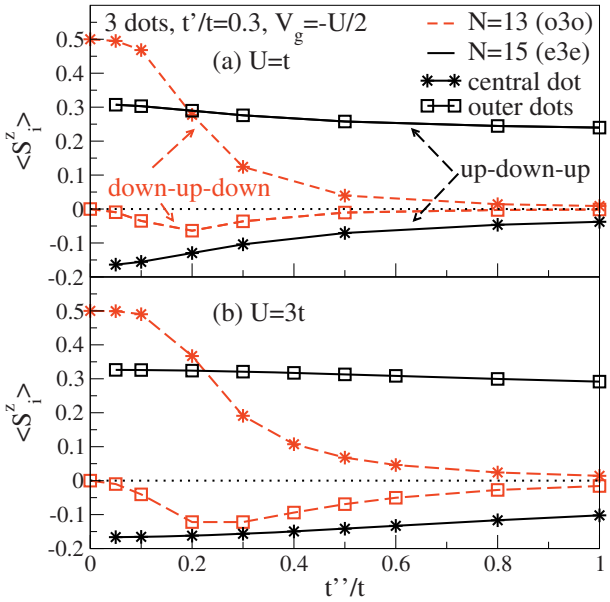

Fig. 9. (Color online) Three dots, $t'/t = 0.3$, $U/t = 1$ (a) and $U/t = 3$ (b). (a) Spin projection $\langle S^z_i \rangle$ vs. t''/t for the outer dots (squares) and the central dot (stars) for $N = 13$ (o3o, dashed lines) and $N = 15$ (e3e, solid lines) clusters. (b) Same as in (a), but for $U/t = 3$. Note that the magnitude of the fixed spins for both clusters (o3o and e3e) increase with the value of U. On o3e clusters, $\langle S^z_{\rm i} \rangle = 0$ (DMRG; $M = 300$).

of $S^z_{\rm total}$ located on the central dot. This cluster type is therefore geometrically similar to the e1e clusters of one quantum dot. As it is illustrated for the case of $t''/t = 0.05$ in Figure 10b, the spin fluctuations on the central dot increase very slowly with system size. We may therefore argue that here the central dot fails to participate in a Kondo effect, especially in the two-stage Kondo regime. This pathology, i.e., the finite $S^z_{\mathbf{D2}}$, is at the origin of the conductance dip at $V_g = -U/2$ observed with ECA in reference [28], similar to the case of one quantum dot.

Clusters with an overall $S^z_{\rm total} = 0$ (i.e., o3e – squares in Figs. 10 and 11) exhibit the least significant finite-size effects and local fluctuations converge the fastest with system size N, while spin-spin correlations exhibit an asymmetry between the left and right lead. As a conclusion, we may expect reliable results for conductances from this cluster type, and this notion will further be corroborated by ECA results in Section 4.2.

4.2 ECA results for the conductance of three dots: comparison of cluster types

4.2.1 Gate-potential dependence

In this section, we present ECA results for the conductance G and $n_{\rm total}$ ($n_{\rm total} = \langle n_{\rm D1} \rangle + \langle n_{\rm D2} \rangle + \langle n_{\rm D3} \rangle$) for the three dots configuration as a function of the gate potential, comparing all three cluster types. The ECA results (solid lines) are depicted in Figures 12a (o3e), 12b (o3o), and 12c (e3e). As expected from the discussion of

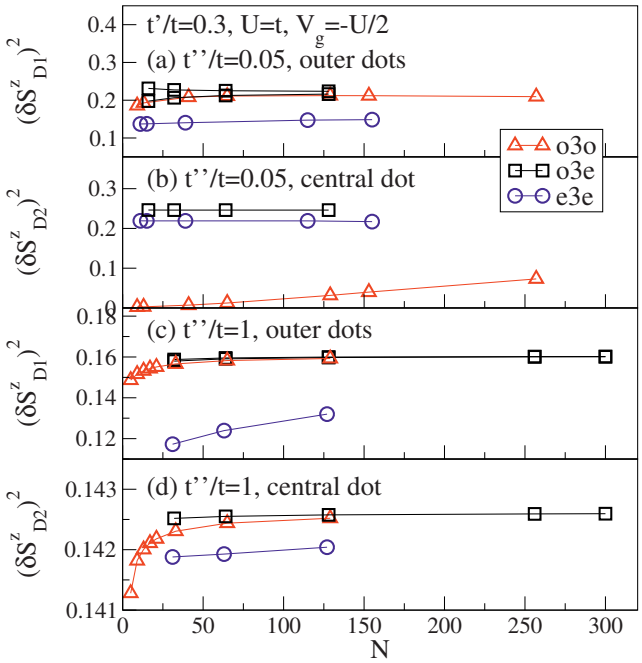

Fig. 10. (Color online) Three dots, $t'/t = 0.3$, $U/t = 1$. Finite-size scaling of spin-fluctuations on the dots for $t''/t = 0.05$ (a, b) and $t''/t = 1$ (c, d). DMRG results for all three cluster types: o3e (squares), e3e (circles), and o3o (triangles) ($M \leq 500$).

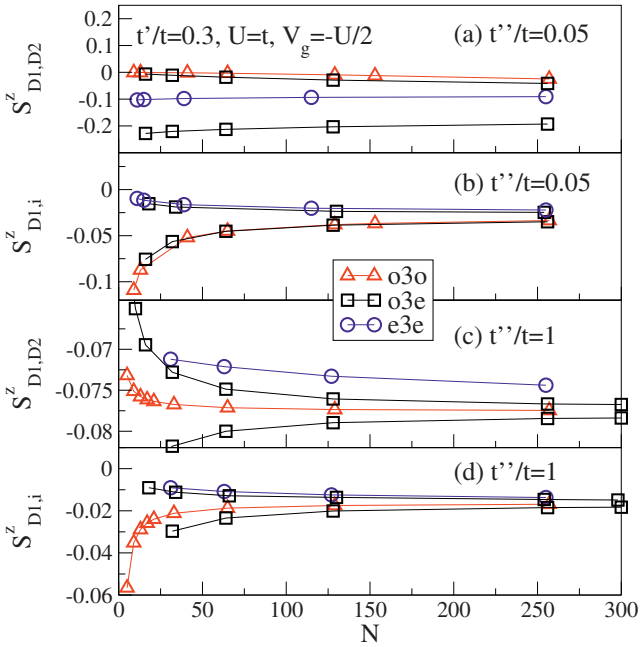

Fig. 11. (Color online) Three dots, $t'/t = 0.3$, $U/t = 1$. Finite-size scaling of spin-spin correlations for $t''/t = 0.05$ (a, b) and $t''/t = 1$ (c, d) (DMRG, $M \leq 500$). (a) and (c) Spin-spin correlations between the central dot and the outer ones. In the o3e case (squares), there are two branches as in reality, we alternate between o3e and e3o (even-dots-odd) configurations as N increases. (b) and (d) Spin-spin correlations between the outer dots and the first site in the adjacent lead. In these two panels and for o3e clusters (squares), the upper(lower) curve shows $S_{\mathbf{D1},i}$ ($S_{\mathbf{D3},i}$).

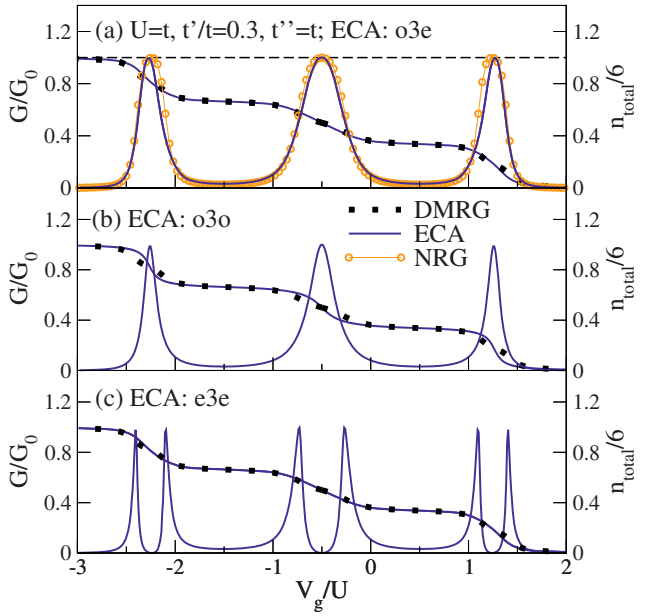

Fig. 12. (Color online) Three dots, $t'/t = 0.3$, $U/t = 1$, $t''/t = 1$. Conductance and charge vs. gate potential V_g/U. (a) ECA results for the conductance and charge for an o3e cluster (solid lines, $N_{\rm ED} = 12$) vs. DMRG results for the charge $n_{\rm total}$ (dotted line, $N = 300$, $M = 400$) and NRG results ([87], circles). (b) ECA results for an o3o cluster (solid lines, $N_{\rm ED} = 9$). (c) ECA results for an e3e cluster (solid lines, $N_{\rm ED} = 11$). DMRG results for $n_{\rm total}$ (dotted line) are included in (b) and (c) for comparison.

static properties in Section 4.1, the results for $n_{\rm total}$ for o3e clusters obtained after embedding agree very well with DMRG results (squares, see Fig. 12a), while the results for the conductance from other clusters deviate strongly from DMRG data (squares, see Figs. 12b and 12c). From Figure 12c (solid lines), we realize that e3e clusters produce the expected Coulomb-blockade like behavior due to the rigid spins on the outer dots (see Fig. 9).

Figure 12a also contains NRG data from reference [87]. The agreement between ECA and NRG [87] is quite good, especially for the central Kondo peak and the Coulomb blockade valleys at $n_{\rm total} = 2, 4$. This clearly establishes that reliable results can be obtained from ECA calculations using o3e clusters.

4.2.2 Behavior at the particle-hole symmetric point

Thus far, we have seen that with o3e clusters, we obtain the best agreement with NRG regarding the gate-potential dependence. Let us next address the value of the conductance at the particle-hole symmetric point as a function of t''. This will indicate what parameter range can be accessed when decreasing t''/t using o3e clusters.

Figure 13 compares o3e and o3o ECA conductance results at $V_g = -U/2$ for $U = t$ and $U = 3t$. In the former case, where o3o clusters with $N_{\rm ED} = 5, 9$ are compared with an o3e cluster with $N_{\rm ED} = 12$, it is shown that there is barely any difference between the results for the two

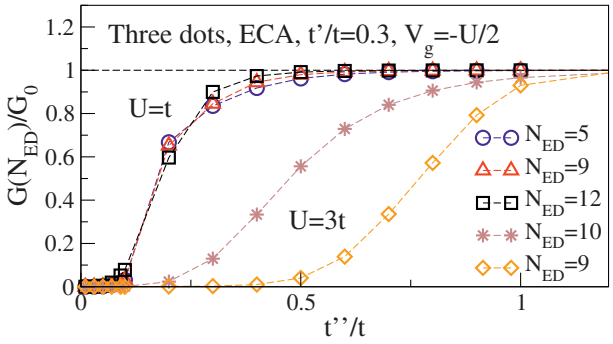

Fig. 13. (Color online) Three dots with $t'/t = 0.3$, $U/t = 1$, and $U/t = 3$: variation of the conductance computed with ECA with t'' at the particle-hole symmetric point $V_g = -U/2$. The results for $U/t = 1.0$ are calculated using o3o with $N = 5$ sites (circles) and $N = 9$ sites (triangles), as well as o3e clusters with $N = 12$ sites (squares). At this value of U/t, there is barely any difference between the two types of clusters, i.e., as the value of t'' increases, the conductance at the particle-hole symmetric point changes from 0 to G_0 at basically the same value of t'', independently of the cluster type. However, the same is not true for the $U/t = 3$ results ($N = 10$ for o3e cluster (stars) and $N = 9$ for o3o cluster (diamonds)). It is clear that the o3o clusters yield a vanishing G at substantially higher t'' than the o3e ones. As explained in the text, this is caused by a larger fixed spin in o3o clusters at higher U values.

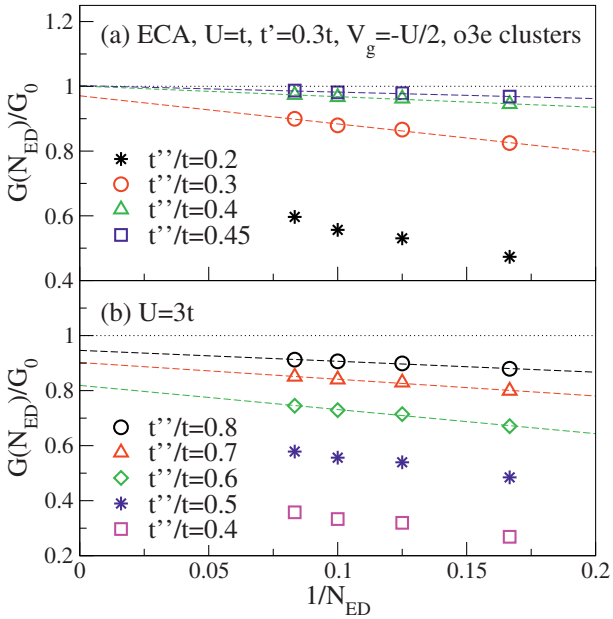

Fig. 14. (Color online) Three dots, $t'/t = 0.3$, $U/t = 1$ (a) and $U/t = 3$ (b). (a) Finite-size scaling analysis of ECA results on o3e clusters for $G(N_{\rm ED})$ at the particle-hole symmetric point ($V_g = -U/2$) for $t''/t = 0.45$, 0.4, 0.3, 0.2 (squares, triangles, circles, and stars). Dashed lines are the linear fits to $G(N_{\rm ED})$. (b) Same as in (a), but now for $U/t = 3$, and $t''/t = 0.8$, 0.7, 0.6, 0.5, and 0.4 (circles, triangles, diamonds, stars, and squares). Note that in this case, the threshold, below which the convergence to G_0 cannot be ascertained, is higher than in the $U/t = 1$ case.

different types of clusters: for $t''/t \approx 0.5$, the correct result $G/G_0 = 1$ is recovered. However, in the later case ($U = 3t$), there is a pronounced difference between o3o ($N_{\rm ED} = 9$) and o3e ($N_{\rm ED} = 10$) results: the vanishing of the conductance at the particle-hole symmetric point for the o3o cluster occurs at a much higher value of t''/t than for the o3e cluster. The reason for that can be understood by analyzing the results in Figure 9, where the fixed net-spin present in o3o clusters is compared for $U = t$ (panel (a)) and $U = 3t$ (panel (b)). A larger value of U, for a fixed t'', increases the magnitude of the fixed spins in the three dots (see Fig. 9). Therefore, as pointed out above, o3e clusters, with $S^z_{\rm total} = 0$, provide better results at the particle-hole symmetric point when compared to o3o clusters. In the next section, we will discuss why the conductance eventually also vanishes for low t'' values in the o3e cluster and numerically accessible values of L, which do not exhibit finite values of $\langle S^z_i \rangle$.

We now turn to a finite-size scaling analysis of $G(N)$ at $V_g = -U/2$. Using cluster sizes within ECA that are numerically tractable (i.e., $N_{\rm ED} \lesssim 13$), we find that, at the particle-hole symmetric point, for $U/t = 1.0$, $G(N_{\rm ED})/G_0$ scales to one with $1/N_{\rm ED}$ for $t''/t \gtrsim 0.3$ (upper panel in Fig. 14). In addition, it is clear from the results shown in Figure 14b that, the larger the value of U, the higher is the value of t'' below which one cannot clearly ascertain the extrapolation of $G(N_{\rm ED})$ to G_0 at small t'' values. Obviously, this happens because the Kondo temperature of the second stage decreases with U, causing the ECA conductance to vanish at a larger t''. Summarizing, both o3o and o3e clusters produce results in qualitative agreement with other techniques at $V_g = -U/2$ above certain values of t''. For $U/t = 1$, $G = G_0$ can be obtained by extrapolation with a $G(N_{\rm ED}) = G_0 - {\rm const.}/N_{\rm ED}$ function for $t''/t \gtrsim 0.2$. For smaller t'', system sizes are too small to establish a clear trend of $G(N_{\rm ED})/G_0$ towards unity due to a finite level spacing.

We are led to conclude that ECA captures quite well the correct physics depending upon the parameters and the cluster taken. The optimum cluster can be identified by analyzing the finite-size scaling of, e.g., the charge, with either the Lanczos solver that is part of ECA or independent techniques such as ground state DMRG, the latter being available in open access releases, of, e.g., the ALPS project [88].

4.3 o3e clusters in the small t'' regime

We next wish to illustrate the finite-size effects encountered in the small t'' regime, for o3e clusters. Unfortunately, when t'' is decreased, the asymmetry between the two outer dots on o3e becomes quite pronounced. Note that the total charge from ECA still agrees well with DMRG down to very small t'' (not shown). However, spin-spin correlations on small o3e clusters suffer from (i) the aforementioned asymmetry between the two outer dots (see Fig. 11) and (ii) the fact that the central dot is basically decoupled from the leads (at the Fermi energy). This is indicated by small spin-spin correlations between

the central dot and the first site in the leads, which indicates that the effective exchange with the leads is smaller than the energy level spacing. Consistent with the first point discussed here, in accordance to the LDOS calculated with ECA for an o3e configuration (not shown), at small t'' and for $V_g = -U/2$ (particle-hole symmetric point), only one of the outer dots develops a sharp Kondo resonance, namely the one connected to the *odd* lead. The dot connected to the *even* lead can only be Kondo screened through the other two dots. However, at low values of t'', this mechanism becomes ineffective and thus the dot's LDOS at the Fermi energy is low, leading to the suppression of the conductance at the particle-hole symmetric point, as seen in Figure 13. Therefore, even for the optimum cluster type o3e, the two-stage Kondo regime seems to be out of reach within the real-space variant of ECA and current computational resources.

5 Summary

In this work, we have performed an extensive finite-size scaling analysis of fluctuations and correlations in nanostructures, such as one and three quantum dots coupled to noninteracting, tight-binding leads. Strong differences in the finite-size scaling behavior emerge depending on even-odd effects [62]. These findings are relevant for the interpretation of results from numerical approaches for the calculation of the conductance of nanostructures that are based on analyzing clusters of finite length with open boundary conditions, such as time-dependent DMRG or the embedded-cluster approximation (ECA). To qualitatively capture precursors of the Kondo effect within these two methods, clusters with a $S^z_{\rm total} = 0$ are best suited, as electrons on the dot at half filling naturally participate in a singlet state. Other cluster types with an overall $S^z_{\rm total} = 1/2$ may be *far* away from capturing Kondo physics in the sense of slow convergence with system size. For certain configurations, most of the $S^z_{\rm total} = 1/2$ is found on the central site, which, if this site is a quantum dot, will cause a gap in the local density of states at the Fermi level, reminiscent of the Zeeman-splitting of the conductance due to the application of a magnetic field.

These findings help to understand the discrepancy between ECA results for three dots and those of other techniques: the vanishing of the conductance at the particle-hole symmetric point obtained with ECA is only seen on certain cluster types, but disappears when the three dots are embedded in a cluster with an overall $S^z_{\rm total} = 0$. In the latter case, the ECA results are then in agreement with the picture proposed in references [36,40,65–69]. While parameter regimes with exponentially small energy scales such as two-stage Kondo regimes are difficult to be accessed with this technique in its real-space variant, very good agreement with exact results such as the Friedel sum rule in the case of one dot – as shown in Figure 8a – or NRG in the case of three dots is otherwise found in other regions of the parameter space. The latter is established from Figures 12a and 13.

Another model that exhibits a two-stage Kondo effect is two dots coupled in a T-shape geometry [86,89]. At half filling, the conductance is found to vanish [86,89], a picture that disagrees with ECA results in the two-stage Kondo regime [79]. We have performed a similar analysis of static properties and ECA results on different cluster types for this geometry, with results not shown here. While in the regime of large t''/U, where t'' is the hopping between the two dots, good agreement between the Friedel sum rule [86] and ECA is found, the two-stage Kondo regime, which emerges at small t'' [86,89] suffers from strong finite-size effects. Unfortunately, no cluster type shows a particularly fast scaling behavior here.

We conclude that the determination of the optimum cluster type is crucial. This can be done by studying different cluster types with the Lanczos solver that is part of standard ECA codes. Further, a comparison of ECA results for static properties, such as the total charge of a nanostructure as a function of gate potential and very importantly, spin and charge fluctuations, against independent techniques, such as ground-state DMRG, is helpful in this respect as well, as we showed in this work. Promising results from a new version of ECA that incorporates a logarithmic discretization of the DOS of the leads clearly indicate that the range of validity of the embedded-cluster approximation can further be improved [84].

It is a pleasure to thank Hsiu-Hau Lin, Volker Meden, Jose Riera, and Marcos Rigol for fruitful discussions. We thank Rok Žitko for providing us with NRG data for three dots. E.V.A. acknowledges support from CNPq and FAPERJ, Brazil. Research at ORNL is sponsored by the Division of Materials Sciences and Engineering, Office of Basic Energy Sciences, U.S. Department of Energy, under contract DE-AC05-00OR22725 with Oak Ridge National Laboratory, managed and operated by UT-Battelle, LLC. K.A.A., E.D., and F.H.-M. are supported in part by NSF grant DMR-0706020. C.A.B. and G.B.M acknowledge support from the NSF (DMR-0710529) and G.B.M. was further supported by Research Corporation (Contract. No. CC6542).

References

1. D. Goldhaber-Gordon, H. Shtrikman, D. Mahalu, D. Abusch-Magder, U. Meirav, M.A. Kastner, Nature **391**, 156 (1998)
2. L. Glazman, M. Raikh, JETP Lett. **47**, 452 (1988)
3. T.K. Ng, P.A. Lee, Phys. Rev. Lett. **61**, 1768 (1988)
4. Y. Meir, P. Lee, Phys. Rev. Lett. **68**, 2512 (1992)
5. L. Glazman, M. Pustilnik, *Nanophysics: Coherence and Transport*, edited by H. Bouchiat et al. (Elsevier, 2005), p. 427
6. M. Pustilnik, Phys. Stat. Sol. (a) **203**, 1137 (2006)
7. M. Grobis, I. Rau, R. Potok, D. Goldhaber-Gordon, *Kondo Effect in Mesoscopic Quantum Dot* (Wiley, 2007)

8. W.G. van der Wiel, S.D. Franceschi, T. Fujisawa, J.M. Elzerman, S. Tarucha, L.P. Kouwenhoven, Science **289**, 2105 (2000)
9. J. Park, A.N. Pasupathy, J.I. Goldsmith, C. Chang, Y. Yaish, J.R. Petta, M. Rinkoski, J.P. Sethna, H.D. Abruna, P.L. McEuen, D.C. Ralph, Nature **417**, 722 (2002)
10. K.G. Wilson, Rev. Mod. Phys. **47**, 773 (1975)
11. H.R. Krishna-murthy, J.W. Wilkins, K.G. Wilson, Phys. Rev. B **21**, 1003 (1980)
12. F.B. Anders, A. Schiller, Phys. Rev. Lett. **95**, 196801 (2005)
13. R. Bulla, T. Costi, T. Pruschke, Rev. Mod. Phys. **80**, 395 (2008)
14. D. Bohr, P. Schmitteckert, P. Wölfle, Europhys. Lett. **73**, 246 (2006)
15. D. Bohr, P. Schmitteckert, Phys. Rev. B **75**, 241103(R) (2007)
16. A. Weichselbaum, F. Verstraete, U. Schollwöck, J.I. Cirac, J. von Delft, e-print `arXiv:cond-mat/0504305` (unpublished)
17. K.A. Al-Hassanieh, A.E. Feiguin, J.A. Riera, C.A. Büsser, E. Dagotto, Phys. Rev. B **73**, 195304 (2006)
18. G. Schneider, P. Schmitteckert, e-print `arXiv:cond-mat/0601389` (unpublished)
19. S. Kirino, T. Fujii, J. Zhao, K. Ueda, J. Phys. Soc. Jpn **77**, 084704 (2008)
20. A. Feiguin, P. Fendley, M.P. Fisher, C. Nayak, Phys. Rev. Lett. **101**, 236801 (2008)
21. E. Boulat, H. Saleur, P. Schmitteckert, Phys. Rev. Lett. **101**, 140601 (2008)
22. L.G.G.V. Dias da Silva, F. Heidrich-Meisner, A.E. Feiguin, C.A. Büsser, G.B. Martins, E.V. Anda, E. Dagotto, Phys. Rev. B **78**, 195317 (2008)
23. S. Weiss, J. Eckel, M. Thorwart, R. Egger, Phys. Rev. B **77**, 195316 (2008)
24. S. Kehrein, Phys. Rev. Lett. **95**, 056602 (2005)
25. V. Ferrari, G. Chiappe, E.V. Anda, M.A. Davidovich, Phys. Rev. Lett. **82**, 5088 (1999)
26. C.A. Büsser, E.V. Anda, A.L. Lima, M.A. Davidovich, G. Chiappe, Phys. Rev. B **62**, 9907 (2000)
27. G. Chiappe, J.A. Verges, J. Phys.: Condens. Matter **15**, 8805 (2003)
28. C.A. Büsser, A. Moreo, E. Dagotto, Phys. Rev. B **70**, 035402 (2004)
29. R. Molina, D. Weinmann, R. Jalabert, G.-L. Ingold, J.-L. Pichard, Phys. Rev. B **67**, 235306 (2003)
30. T. Rejec, A. Ramšak, Phys. Rev. B **68**, 035342 (2003)
31. V. Meden, U. Schollwöck, Phys. Rev. B **67**, 193303 (2003)
32. A. Kaminski, Y.V. Nazarov, L.I. Glazman, Phys. Rev. B **62**, 8154 (2000)
33. A. Rosch, J. Kroha, P. Wölfle, Phys. Rev. Lett. **87**, 156802 (2001)
34. B. Doyon, N. Andrei, Phys. Rev. B **73**, 245326 (2006)
35. H. Schoeller, J. König, Phys. Rev. Lett. **84**, 3686 (2000)
36. C. Karrasch, T. Enss, V. Meden, Phys. Rev. B **73**, 235337 (2006)
37. S.G. Jakobs, V. Meden, H. Schoeller, Phys. Rev. Lett. **99**, 150603 (2007)
38. G. Kotliar, A.E. Ruckenstein, Phys. Rev. Lett. **57**, 1362 (1986)
39. O. Gunnarsson, K. Schönhammer, Phys. Rev. B **31**, 4815 (1985)
40. R. Žitko, J. Bonča, A. Ramšak, T. Rejec, Phys. Rev. B **73**, 153307 (2006)
41. *Time-Dependent Density-Functional Theory*, Lecture Notes in Physics, edited by M.A.L. Marques et al. (Springer, Berlin, 2006), Vol. 706
42. M. Koentopp, K. Burke, F. Evers, Phys. Rev. B **73**, 121403 (2006)
43. A. Arnold, F. Weigend, F. Evers, J. Chem. Phys. **126**, 174101 (2007)
44. P. Schmitteckert, F. Evers, Phys. Rev. Lett. **100**, 086401 (2008)
45. M. Brandbyge, J.-L. Mozos, P. Ordejón, J. Taylor, K. Stokbro, Phys. Rev. B **65**, 165401 (2002)
46. K.A. Al-Hassanieh, C.A. Büsser, G.B. Martins, E. Dagotto, Phys. Rev. Lett. **95**, 256807 (2005)
47. G.B. Martins, C.A. Büsser, K.A. Al-Hassanieh, E.V. Anda, A. Moreo, E. Dagotto, Phys. Rev. Lett. **76**, 066802 (2006)
48. C.A. Büsser, G.B. Martins, Phys. Rev. B **75**, 045406 (2007)
49. G.B. Martins, C.A. Büsser, K.A. Al-Hassanieh, A. Moreo, E. Dagotto, Phys. Rev. Lett. **94**, 026804 (2005)
50. S.R. White, Phys. Rev. Lett. **69**, 2863 (1992)
51. S.R. White, Phys. Rev. B **48**, 10345 (1993)
52. U. Schollwöck, Rev. Mod. Phys. **77**, 259 (2005)
53. K. Hallberg, Adv. Phys. **55**, 477 (2006)
54. J.E. Gubernatis, J.E. Hirsch, D.J. Scalapino, Phys. Rev. B **35**, 8478 (1987)
55. W.B. Thimm, J. Kroha, J. von Delft, Phys. Rev. Lett. **82**, 2143 (1999)
56. E.S. Sørensen, I. Affleck, Phys. Rev. Lett. **94**, 086601 (2005)
57. S. Costamagna, C. Gazza, M. Torio, J.A. Riera, Phys. Rev. B **74**, 195103 (2006)
58. L. Borda, Phys. Rev. B **75**, 041307 (2007)
59. N. Andrei, Phys. Rev. Lett. **45**, 379 (1980)
60. U. Gerland, J. von Delft, T.A. Costi, Y. Oreg, Phys. Rev. Lett. **84**, 3710 (2000)
61. A. Hewson, *The Kondo Problem to Heavy Fermions* (Cambridge, UK, 1993)
62. E.S. Sørensen, I. Affleck, Phys. Rev. B **53**, 9153 (1996)
63. T.-S. Kim, S. Hershfield, Phys. Rev. B **65**, 214526 (2002)
64. T. Hand, J. Kroha, H. Monien, Phys. Rev. Lett. **97**, 136604 (2006)
65. A. Oguri, Phys. Rev. B **59**, 12240 (1999)
66. A. Oguri, A.C. Hewson, J. Phys. Soc. Jpn **74**, 988 (2005)
67. R. Žitko, J. Bonča, Phys. Rev. Lett. **98**, 047203 (2007)
68. Y. Nisikawa, A. Oguri, Phys. Rev. B **73**, 125108 (2006)
69. A.M. Lobos, A.A. Aligia, Phys. Rev. B **74**, 165417 (2006)
70. T. Kuzmenko, K. Kikoin, Y. Avishai, Europhys. Lett. **64**, 218 (2003)
71. S.R. White, A.E. Feiguin, Phys. Rev. Lett. **93**, 076401 (2004)
72. A. Daley, C. Kollath, U. Schollwöck, G. Vidal, J. Stat. Mech.: Theory Exp. P04005 (2004)
73. E.V. Anda, J. Phys. C **14**, 1037 (1981)
74. W. Metzner, Phys. Rev. B **43**, 8549 (1991)
75. M.A. Davidovich, E.V. Anda, C.A. Büsser, G. Chiappe, Phys. Rev. B **65**, 233310 (2002)

76. E.V. Anda, C.A. Büsser, G. Chiappe, M.A. Davidovich, Phys. Rev. B **66**, 035307 (2002)
77. G. Chiappe, E. Louis, E.V. Anda, J.A. Verges, Phys. Rev. B **71**, 241405(R) (2005)
78. J.M. Aguiar-Hualde, G. Chiappe, E. Louis, E.V. Anda, Phys. Rev. B **76**, 155427 (2007)
79. C.A. Büsser, G.B. Martins, K. Al-Hassanieh, A. Moreo, E. Dagotto, Phys. Rev. B **70**, 245303 (2004)
80. N.S. Wingreen, A.-P. Jauho, Y. Meir, Phys. Rev. B **48**, 8487 (1993)
81. A. Schiller, S. Hershfield, Phys. Rev. B **62**, R16271 (2000)
82. M.A. Cazalilla, J.B. Marston, Phys. Rev. Lett. **88**, 256403 (2002)
83. K.A. Al-Hassanieh et al., unpublished results
84. E.V. Anda, G. Chiappe, C.A. Büsser, M.A. Davidovich, G.B. Martins, F. Heidrich-Meisner, E. Dagotto, Phys. Rev. B **78**, 085308 (2008)
85. E. Lieb, F.Y. Wu, Phys. Rev. Lett. **20**, 1445 (1968)
86. P.S. Cornaglia, D.R. Grempel, Phys. Rev. B **71**, 075305 (2005)
87. R. Žitko, unpublished results
88. A. Albuquerque, F. Alet, P. Corboz, P. Dayal, A. Feiguin, S. Fuchs, L. Gamper, E. Gull, S. Guertler, R. Igarashi, M. Koerner, A. Kozhevnikov, A. Laeuchli, S. Manmana, M. Matsumoto, I. McCulloch, F. Michel, R. Noack, G. Pawlowski, L. Pollet, T. Pruschke, U. Schollwöck, S. Todo, S. Trebst, M. Troyer, P. Werner, S. Wessel, J. Mag. Mag. Mat. **310**, 1187 (2007)
89. R. Žitko, J. Bonča, Phys. Rev. B **73**, 035332 (2006)